Magnetic Resonance Imaging of Structure and Coarsening in Three-Dimensional Foams

Burkhard A. Prause and James A. Glazier
Department of Physics, University of Notre Dame, Notre Dame, IN 46556

We used Magnetic Resonance Imaging (MRI) to study non-destructively the interior of slowly coarsening disordered foams. We developed two methods for data analysis that can independently provide detailed structural information, including the distributions of bubble sizes, faces per bubble and edges per face to study foams with varying liquid fractions and polydispersity.

We analyzed several hundred bubbles in detail, and found neither Kelvin nor complete Weaire-Phelan polyhedral structures.

Our analysis provided values for the average number of faces, $\langle f \rangle$, the averaged zero growth value, f_0, and the volume rate of change for individual bubbles with constant topology. While the average volume rate of change depends on the initial disorder and wetness, the growth rate for each foam is compatible with Glazier's linear three-dimensional growth law.

Neither foam coarsened self-similarly during an average volume increase of a factor of 3.5 agreeing with simulation results that equilibration is very slow in three-dimensional foams.

I. INTRODUCTION

Early this century D'Arcy Thompson [1] attributed the formation of many regular biological patterns, such as the bee's honeycomb, sponges and cucumber skin, to the action of purely physical forces, stressing the analogy between the development of foam structure and the formation of other natural patterns. Smith noted the similar nature of coarsening in bubbles and growth in metallic grains [2], proposing foams as a convenient model for the universal dynamics of grain growth. Today, foam experiments model cellular materials in two and three dimensions, in which simple physical constraints, such as diffusion and surface energy minimization drive structure and dynamics. Industries including brewing, printing, fire-fighting and oil exploration all use foams.

Recent simulations have led to a better theoretical understanding of three-dimensional growth laws and the scaling properties of grains [3–6]. Analogous to von Neumann's law for two-dimensional grain growth [7], based on computer simulations, Glazier proposed an averaged growth law for three-dimensional grains [3]:

$$\langle \mathrm{V}_f \rangle^{-1/3} \langle \frac{\mathrm{dV}_f}{\mathrm{dt}} \rangle = k(f - f_0). \tag{1}$$

The averaged volume rate of change for a group of bubbles with f faces depends only on its number of faces. On average, bubbles with f greater than f_0 will grow, while bubbles with a smaller number of faces will shrink. k is a diffusion constant. For the relation between f and f_0 , Weaire and Glazier deduced that [4]:

$$f_0 = \langle f \rangle \left(1 + \frac{\mu_2}{\langle f \rangle^2} \right), \tag{2}$$

where $\mu_2 = \langle f^2 \rangle - \langle f \rangle^2$ measures the disorder of the foam. Eqn. 2 is exact provided that the average volume of a bubble with f faces scales as $\langle V_f \rangle \propto f^3$, which was true in Glazier's Potts model simulations.

A large amount of work addresses the minimal surface area partition of three-dimensional space into polyhedral domains of uniform volume. Weaire and Phelan recently showed that the β-Tungsten lattice partition with a unit cell composed of a regular pentagonal dodecahedron and six tetrakaidecahedral barrels (with two hexagonal faces and twelve pentagonal faces) has a lower surface area than a partition into regular Kelvin tetrakaidecahedra (six square faces and eight hexagonal faces) [8–10].

Experimental verification of the existence of any of these structures in bulk three-dimensional foams has proven difficult, in part due to the difficulty of visualizing the foam interior. Both structures can occur in foams confined to tubes narrow compared to the typical bubble radius.

Durian *et al.* used diffusing wave spectroscopy (**DWS**) to measure the rates of rearrangement and the averaged grain volume growth exponents in bulk shaving cream [11–13]. They found that the average radius grew according to a power law $\langle r \rangle \propto t^{\beta}$, with $\beta = 0.5$, consistent with "self-similar" growth, in which the normalized distribution of bubble volumes does not change over time. DWS cannot provide direct information on bubble size distributions or grain shapes and topologies which are needed to verify growth laws, but it can examine very large numbers of bubbles (hundreds of thousands) over many decades of growth in length scale.

Confocal optical tomography (**COT**) can determine the growth and shapes of individual bubbles in dry foams [14,15], but only for foams with a few interior bubbles (Monnereau *et al.* studied a total of 28). COT is anisotropic with limited spatial resolution, and requires black film boundaries, which restricts it to extremely dry foams.

The botanist Matzke made the most careful study of three dimensional bubble shapes, using a simple binocular microscope [16,17] and near endless patience. He studied 1000 individual bubbles, noting their numbers of faces and edges. While providing valuable data on the shapes of such grains, he could

not provide information on volumes, lacking the ability to determine exact vertex locations, or to track a bubble's evolution over time.

Magnetic Resonance Imaging provides detailed information on the structure and evolution of individual bubbles in a large variety of foams.

II. MRI EXPERIMENTS

MRI has evolved into a widely used and irreplaceable tool in diagnostic medicine since its discovery in 1973 [18]. It detects the precessing magnetic moments of excited nuclei in the presence of magnetic field gradients, making it ideal to study biological tissues which contain a high natural abundance of excitable water [19]. Non-medical MRI has developed comparatively slowly, due to the varying requirements of different physical, chemical and material science applications, which require custom imaging techniques and high performance imagers and computers [20,21].

German *et al.* made the first MRI foam images [22], investigating foam drainage by measuring the water content inside a column of liquid foam over time. The two-dimensional images could only distinguish a few very large bubbles. Gonatas *et al.* succeeded in imaging two-dimensional slices, measuring the bubble size distributions over long periods of time [23]. Their foam did not reach self-similar growth (the scaling state), having a growth exponent, $\beta = 0.3$.

Our experiments used a gelatin based liquid with SDS as surfactant and trace amounts of $CuSO_4$ and $DyCl_3$(TTHA) as relaxation agents. We used a 7 Tesla SQUID magnetometer to measure the magnetization of the liquid with varying amounts of relaxation agents. Matching the magnetic susceptibility of the liquid to that of air minimized susceptibility artifacts in the foam during imaging, as well as increasing the susceptibility induced transverse relaxation time T_2 [20].

We produced foams by two methods, resulting in different degrees of initial wetness and polydispersity. Blowing air through a millipore (fish-tank) filter produced very dry (volume liquid fraction $\Phi = 3\%$) foam, with an initial average bubble diameter of 2.0mm $\pm$ 0.3mm. By whipping the liquid with an electric mixer, we obtained an initially wet ($\Phi = 50\%$) foam, which drained to about $\Phi = 10\%$ after 90 minutes, resulting in a moderately dry polyhedral foam, with bubble diameters ranging from 30μm to 300μm.

Due to the non-zero liquid fraction, gravitational drainage of liquid through Plateau borders and edges affects coarsening in the foam, as well as gas diffusion across the films, vertex coalescence and wall breakage. Holding the sealed glass cells containing the foam at a constant temperature of 280°K, limited the rate of drainage and kept air from drying the foam walls. Samples prepared in this manner coarsened without breaking down for as long as six days, at which time the gelatin in the faces started polymerizing, inhibiting growth.

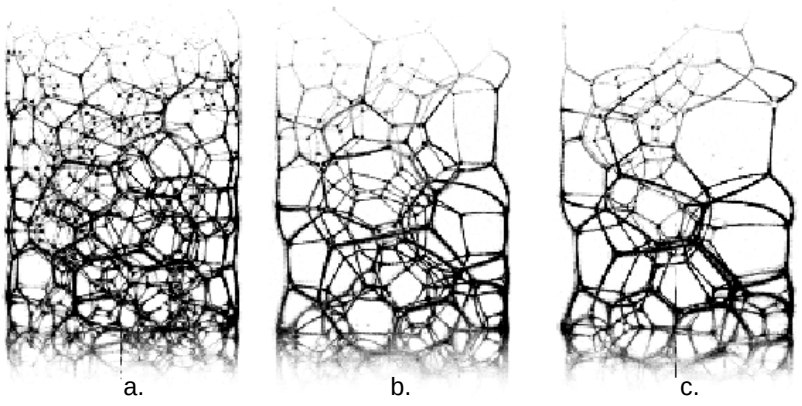

FIG. 1. Maximum intensity projections of three-dimensional MRI reconstructions of a foam at three stages of development. (a) = 24 hrs. (b) = 36 hrs. (c) = 48 hrs.

The stability and magnetic homogeneity of the samples allowed us to image the foams in three dimensions, using our own Bruker 300 MHz (7 Tesla) imaging spectrometer and a set of water-cooled high field gradients (96 G/cm), to achieve sufficient spatial resolution in this strongly relaxing material. The samples were placed inside 15mm or 25mm rf-coils and kept at constant 280°K±1°K. A customized 3D spin-echo pulse sequence with very high repetition rates (TE = 1.9ms, TR = 50ms) provided $256 \times 128 \times 128$ real data points, at isotropic resolutions of 101μm in the 15mm coil, and 140μm in the 25 mm coil. A single average of the entire sample took 14 minutes. To improve the signal to noise ratio, initial scans employed two averages, extended to four and later eight, as the sample drained. Thus a "snapshot" of the foam took 30 minutes initially (for about 24 hours) and 120 minutes at the end of the run. We took data for both relatively homogeneous (first method) and polydisperse (second method) foams in both rf-coils. The larger volume of the 25mm coil allowed the foam to coarsen to a longer length scale but reduced the signal intensity, which is twice as great in the 15mm coil. Figure 1 shows three-dimensional, maximum intensity reconstructions of a dry, initially homogeneous foam at different stages of development.

III. ANALYSIS

We have developed two methods to analyze the three-dimensional data sets. The more labor intensive method concentrates on exact reconstruction of each

individual bubble. We cut the data run into slices one pixel deep. The images show signal along all intersections of bubble faces (edges). Scanning through the slices, we identify any point at which four edges converge as a vertex and record its location. We process the lists of vertices that belong to each bubble using the qhull algorithm [24] (qhull is available for free from the University of Minnesota Geometry Center), creating a list of simplicial (triangular) facets that constitute the smallest convex hull around the set of vertices. From this list we calculate the bubble volumes. We then merge the facets to create non-simplicial faces that have the same number of edges as the corresponding polygonal walls of the bubbles. This method allows us to investigate the detailed shapes of any number of interior bubbles, limited only by the cumbersome procedure of tracing all vertices in the sample. We analyzed over 300 bubbles at different stages of coarsening between 24 and 48 hours. We found no Kelvin tetrakaidecahedra, or full Weaire-Phelan structures, but did find six pentagonal dodecahedra. Only two dodecahedra were present in the sample at the same time and they did not adjoin tetrakaidecahedral barrels. At 36 hours, the mean number of edges per face was $\langle n \rangle = 5.06$, and the mean number of faces $\langle f \rangle = 12.32 \pm 0.56$.

Fig. 2(a) shows the averaged volume for f-faced bubbles as a function of the number of faces for a 36 hour foam. Fig. 2 shows the distributions of (b) volumes, (c) numbers of edges and (d) numbers of faces. For $\langle V_f \rangle \propto f^{\alpha}$, we found $\alpha = 2.7 \pm 0.36$, consistent with the value for Potts model simulations, $\alpha = 3$ [4]. Using Eqn. 2 we found a zero growth value $f_0 = 16.3 \pm 0.74$, consistent with $f_0 = 15.8$ for the Potts model [3]. The disorder was $\mu_2(f) = 54$. Manual reconstruction allows us to trace even the smallest polygonal shapes in the samples, with volumes as low as 36 voxels, providing a high degree of accuracy for very polydisperse foams.

We developed a second method to eliminate the manual identification of vertices. We first processed the reconstructed three-dimensional images to remove all imaging artifacts and random noise. Artifact correction employed an appropriate neighborhood ranking filter [25]. To avoid eliminating vertex or edge signal, while removing all disconnected noise ("buckshot") we created a binary image by thresholding and used a closing operator to fill small gaps. A scanning program then recorded the locations of all pixels neighboring at least one voxel with signal. Fig. 3 shows the result of this process on a slice from a three-dimensional data set. We used the list of connected voxels to create a Euclidean distance map of the lattice as shown in Fig. 4, in which the intensity at each voxel is the Euclidean distance to the nearest voxel containing signal.

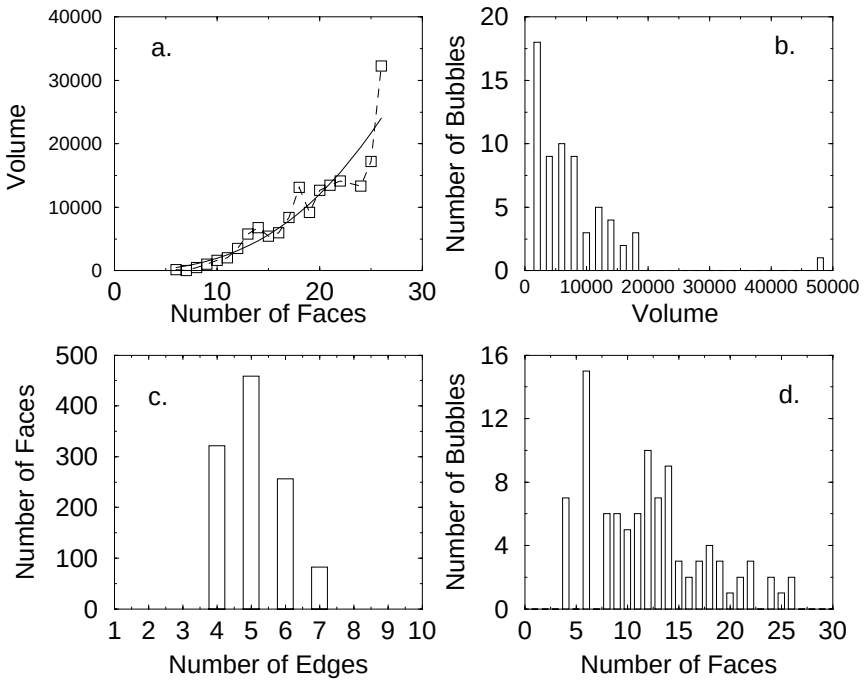

FIG. 2. Detailed structural information from a single data run for a dry foam ($\Phi < 3\%$) at t = 36 hrs. (a) $\langle V_f \rangle$ vs. f. The exponent $\alpha = 2.7$. Distributions of: (b) Volumes. (c) Edges. (d) Faces. Distributions (b) and (d) are wider than at early times, when the foam is much more ordered.

Next we group localized clusters of local maxima into single centers using a third nearest neighbor scan. We eliminate spurious maxima that can occur at the centers of bubble faces by requiring a zero overlap between the zones of influence of all pairs of maxima, imposing the geometric constraint that the diameters of adjacent bubbles are larger than that of their joining face. We use a three-dimensional Delauney triangulation [26] from the center locations to compute neighbors for each center and estimate the averaged radius of the equivalent sphere for each center as the mean of the distances to all its neighbors, weighted by the ratio of the distances between the center and each neighbor. This approximation is the chief source of error in our volume determination. Finally, we discard bubbles in contact with an outside wall or the edge of the image.

We could thus track individual bubbles over time, identifying bubbles that did not change their number of faces between consecutive images. For each time step we compared the centers to those in the previous image and de-

termined the most probable pairings according to center location, volume and number of faces. Between consecutive time steps, only 10 to 15% of all bubbles did not change their number of sides. Of those, we could uniquely map the center locations of over 90%. This information provides f_0 in Eqn. 1 directly. Integrating Eqn. 1 for constant topology yields, for the volume rate of change:

$$\frac{\mathrm{dV}_f^{2/3}}{\mathrm{dt}} = \kappa(f - f_0). \tag{3}$$

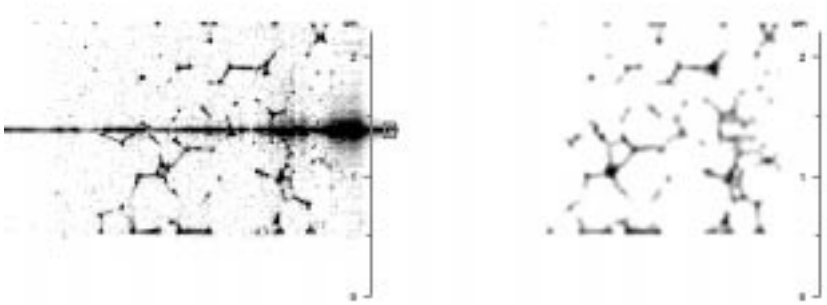

FIG. 3. Left: center slice of a reconstructed foam, showing artifacts and noise. Right: The same image after processing to remove random noise and artifacts.

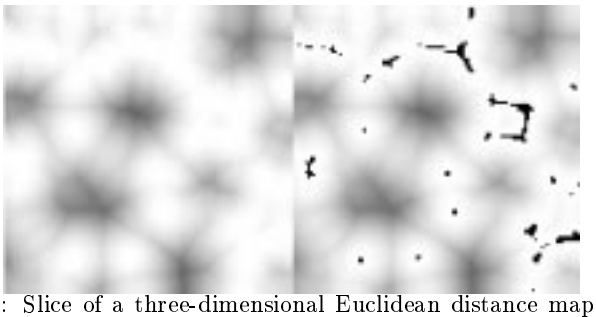

FIG. 4. Left: Slice of a three-dimensional Euclidean distance map. Right: The same map superposed on the corresponding raw image slice in a late stage foam. Darker pixels are farther from the nearest fluid edge.

Fig. 5 shows the volume rate of change as a function of f for two different foam samples. The first sample, foam-10-16 was an initially ordered, very dry foam with $\Phi < 3\%$, while the second sample, foam-2-02 was very polydisperse and relatively wet ($\Phi_0 \sim 10\%$). The zero growth values were $f_0 = 11.6 \pm 3.8$ and $f_0 = 12.1 \pm 3.3$, with $\langle f \rangle = 12.32 \pm 0.69$ and $\langle f \rangle = 12.77 \pm 0.74$, respectively.

The large errors in f_0 are due to the small number of bubbles that maintained a constant f between consecutive time steps. During a series of 36 runs the number of interior bubbles decreased from over 200 to about 40. The values are in very good agreement with each other. They are lower but within error of the values for $\langle f \rangle$ and f_0 found by optical tomography [14] and in simulations [3]. The linearity of the computed derivative in f strongly supports the linear dependence on topology of Glazier's growth law, Eqn. 3. While the large error in our volume determination makes it difficult to determine whether the scatter in growth rate is intrinsic or due to measurement error, the fact that the linearity is better than would be expected from a random error suggests that the volume scatter is intrinsic, *i.e.* that the law holds only on average as in the Potts model.

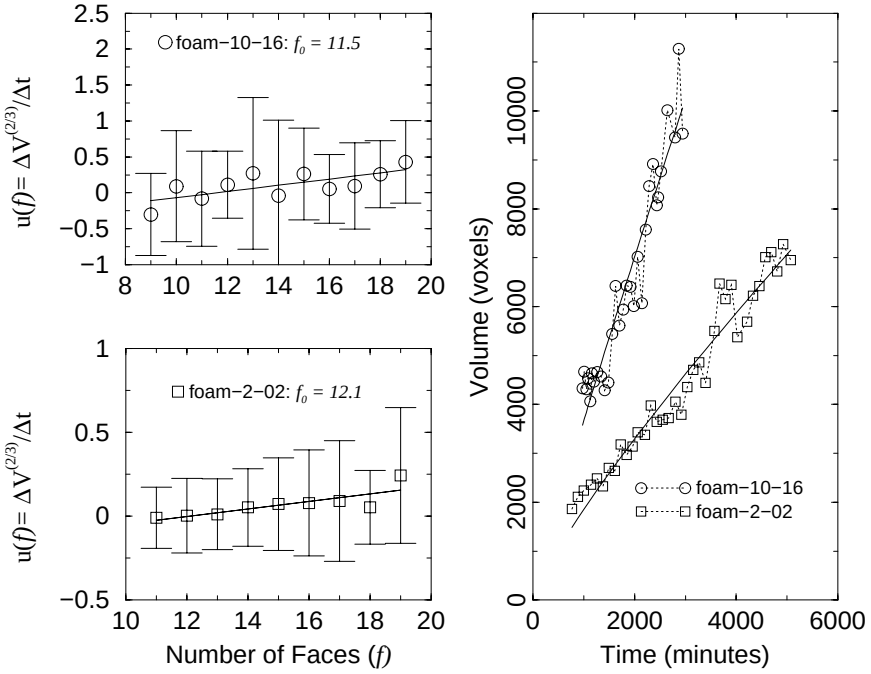

FIG. 5. Left: Time averaged volume rate of change as a function of number of faces, f, for two foams. Right: $\langle V(t) \rangle$ for the same two foams. The different slopes are proportional to the diffusion coefficients in the foams.

For comparison we used Eqn. 2 to compute the zero growth value for the two foams at each time step. Averaged over time we calculated $f_0 = 14.07 \pm 0.25$ for foam-01-16 and $f_0 = 14.88 \pm 0.48$ for foam-2-02. The values for f_0 found by the

two methods for both samples are consistent with each other, due to the large error of the computation using Eqn. 3. The slope $\kappa = 4.31 \times 10^{-2} \pm 1.43 \times 10^{-2}$ mm^2/hr for foam-10-16 was nearly twice as large as the $\kappa = 2.24 \times 10^{-2} \pm 6.0 \times 10^{-3}$ mm^2/hr for foam-2-02. κ is proportional to the diffusion constant, k, in Eqn. 1, which we expected to be lower than for foam-2-02, due to foam-2-02's larger liquid fraction.

Fig. 5 suggests that neither foam reached a scaling state, where $\langle V(t) \rangle \propto t^{\alpha}$, with $\alpha = 1.5$. During coarsening over an average volume increase by a factor of 3.5 in both samples, we found $\alpha = 0.834 \pm 0.055$ in foam-10-16, and $\alpha = 0.936 \pm 0.029$ in foam-2-02. This result is consistent with earlier findings in three-dimensional foams [23,14], and predictions from computer simulations, that disordered three-dimensional foams need several orders of magnitude of length scale coarsening to attain self-similar growth [3].

IV. CONCLUSIONS

We have used MRI to analyze the detailed interior structure of a cellular material, and experimentally verified its dynamics. The data presented are consistent with Glazier's growth law and predictions concerning scaling behavior in three-dimensional foams. They also agree with earlier optical studies on disordered foam structures by Matzke and Monnereau [16,17,15]. We did not find Kelvin tetrakaidecahedra or Weaire-Phelan structures.

Both of our methods for analyzing three-dimensional foam structure have advantages. Hand tracing distinguishes very small bubbles, with volumes near the MRI resolution limit. It also allows faithful reconstruction of bubble shapes. Values for $\langle f \rangle$, f_0, and growth exponents $V(f)$ and $V(t)$, are highly accurate. The method is too labor intensive to determine the time evolution of large numbers of bubbles.

The automated analysis using Euclidean distance maps and Delauney triangulations is computation intensive. Its current implementation loses small bubbles because it requires absolutely noise free data. In future experiments we can improve the large error bars for $\langle f \rangle$ and f_0 by slowing coarsening rates and further reducing imaging times (with minimal loss of signal to noise ratio). Faster imaging will allow us to track more bubbles between rearrangements, improving statistics.

To improve our volume estimates, we are currently incorporating a three-dimensional Voronoi tessellation [26] into our automated analysis, to reconstruct exact hulls around individual bubbles as in our manual method.

ACKNOWLEDGMENTS

This research was supported by NSF/DMR92-57011, NSF/CTS-9601691

and NSF/INT-96-03035-0C, by the American Chemical Society/Petroleum Research Fund, NASA grant UGA99-0083 and DOE grant DE-FG0299ER-45785. We thank Dr. Dieter Gross at Bruker Analytik in Germany for his vital help with the imaging experiments.

---

[1] D. W. Thompson, *On Growth and Form* (Cambridge University Press, Cambridge, 1942).
[2] C. S. Smith, in *Metal Interfaces* (American Society for Metals, Cleveland, 1952), pp. 65–108.
[3] J. A. Glazier, Phys. Rev. Lett. **70**, 2170 (1993).
[4] D. Weaire and J. A. Glazier, Phil. Mag. Lett. **68**, 363 (1993).
[5] C. Sire, Phys. Rev. Lett. **72**, 420 (1994).
[6] R. M. C. de Almeida and J. C. M. Mombach, Physica A **236**, 268 (1997).
[7] J. von Neumann, in *Metal Interfaces* (American Society for Metals, Cleveland, 1952), pp. 108–110.
[8] D. Weaire and R. Phelan, Phil. Mag. Lett. **69**, 107 (1994).
[9] D. Weaire and R. Phelan, Phil. Trans. R. Soc. Lond. A **354**, 1989 (1996).
[10] D. Weaire, *The Kelvin Problem* (Taylor& Francis, London, 1996).
[11] D. J. Durian, D. A. Weitz, and D. J. Pine, J. Phys. Condens. Matt. **2**, SA433 (1990).
[12] D. J. Durian, D. A. Weitz, and D. J. Pine, Science **252**, 686 (1991).
[13] D. J. Durian, D. A. Weitz, and D. J. Pine, Phys. Rev. A **44**, R7902 (1991).
[14] C. Monnereau and M. Vignes-Adler, Phys. Rev. Lett. **80**, 5228 (1998).
[15] C. Monnereau and M. Vignes-Adler, J. Colloid Interface Sci. **202**, 45 (1998).
[16] E. B. Matzke, Am. J. Bot. **33**, 58 (1946).
[17] E. B. Matzke, Am. J. Bot. **33**, 130 (1946).
[18] P. C. Lauterbur, Nature **242**, 190 (1973).
[19] P. Mansfield and P. Morris, *NMR Imaging in Biomedicine* (Academic Press, New York, 1982).
[20] P. T. Callaghan, *Principles of Nuclear Magnetic Resonance Microscopy* (Clarendon Press, Oxford, 1991).
[21] R. A. Komoroski, Analytical Chemistry **65**, 1068A (1993).
[22] J. B. German and M. J. McCarthy, J. Agric. Food Chem. **37**, 1321 (1989).
[23] C. P. Gonatas *et al.*, Phys. Rev. Lett. **75**, 573 (1995).
[24] C. B. Barber, D. P. Dobkin, and H. T. Huhdanpaa, ACM Transactions on Mathematical Software **22**, 469 (1996).
[25] J. C. Russ, *The Image Processing Handbook* (CRC Press, Boca Raton, 1995).
[26] F. Aurenhammer, ACM Computing Surveys **23**, 345 (1991).